PNAS RESEARCH ARTICLE | ENGINEERING

# Nonspherical ultrasound microbubbles

Anshuman Dasgupta[a,b,c,1], Tao Sun[b,c,d,1], Roberto Palomba[e], Elena Rama[a], Yongzhi Zhang[d], Chanikarn Power[d], Diana Moeckel[a], Mengjiao Liu[a], Apoorva Sarode[b], Marek Weiler[a], Alessandro Motta[a], Céline Porte[a], Zuzanna Magnuska[a], Asmaa Said Elshafei[a], Roman Barmin[a], Adam Graham[b], Arthur McClelland[b], Dirk Rommel[f,g], Elmar Stickeler[h], Fabian Kiessling[a], Roger M. Pallares[a], Laura De Laporte[f,g,i], Paolo Decuzzi[e], Nathan McDannold[d], Samir Mitragotri[b,c,2], and Twan Lammers[a,2]

Edited by Joseph DeSimone, Stanford University, Stanford, CA; received November 5, 2022; accepted February 22, 2023

**Surface tension provides microbubbles (MB) with a perfect spherical shape. Here, we demonstrate that MB can be engineered to be nonspherical, endowing them with unique features for biomedical applications. Anisotropic MB were generated via one-dimensionally stretching spherical poly(butyl cyanoacrylate) MB above their glass transition temperature. Compared to their spherical counterparts, nonspherical polymeric MB displayed superior performance in multiple ways, including i) increased margination behavior in blood vessel–like flow chambers, ii) reduced macrophage uptake in vitro, iii) prolonged circulation time in vivo, and iv) enhanced blood–brain barrier (BBB) permeation in vivo upon combination with transcranial focused ultrasound (FUS). Our studies identify shape as a design parameter in the MB landscape, and they provide a rational and robust framework for further exploring the application of anisotropic MB for ultrasound-enhanced drug delivery and imaging applications.**

microbubbles | nonspherical | ultrasound | sonoporation | shape

Microbubbles (MB) are 1- to 10-μm-sized gas-filled vesicles that are shell-stabilized by lipids, polymers, or proteins (1, 2). MB are extensively used in the clinic for ultrasound (US) imaging and drug delivery purposes. MB cause acoustic backscatter, resulting in high echogenicity and thereby providing contrast for functional and molecular US imaging (2, 3). With regard to drug delivery, MB oscillation and/or implosion in response to US excitation results in shear forces in blood vessels and near cell membranes, thereby promoting vascular permeability and drug uptake (4–6). To boost US imaging and drug delivery performance, several design features of MB have been systematically studied, including size, shell composition, shell functionalization, and shell elasticity (7–11).

Shape is an unexplored MB property that may open unique properties for biomedical applications. In contrast to state-of-the-art (pre)clinical MB, which are all spherical in shape, we hypothesized that anisotropy may beneficially impact MB flow dynamics and sonopermeation efficacy (12, 13). First, anisotropic MB are expected to increasingly tumble in blood flow and as a result present with a higher margination propensity, i.e., with an increased tendency to flow closer to blood vessel walls. Second, nonspherical MB may present with reduced phagocyte uptake kinetics, alike nonspherical nanoparticles (14, 15), thereby prolonging their in vivo circulation times. Third, because of enhanced margination and prolonged circulation, the sonopermeation performance of anisotropic MB is expected to be significantly improved.

No preclinical or clinical MB formulation is anisotropic in shape. The key reason for this is that among all geometrical shapes, spheres have the lowest surface-area-to-volume ratio and are thus energetically the most favorable. This natural phenomenon of surface tension gives MB their perfect spherical shape (16). To generate anisotropic MB, external energy must be applied to spherical MB to manipulate their shape. In this regard, film-stretching technology uses thermal and mechanical energy to deform spherical nanoparticles into nonspherical shapes (17, 18). Given its versatile and scalable nature, we deduced that film-stretching technology is a suitable methodology for generating anisotropic MB.

Using film stretching, we set out to produce rod-shaped MB since rods are among the most prevalent anisotropic shapes in nature and in material science (18). We chose to use polymeric MB in spite of the fact that these are known to be somewhat less echogenic and biocompatible than lipid-based MB (3). This was done because polymeric materials enable shape manipulation upon transforming into a soft rubbery state and subsequently enable preservation of the deformed shape by transitioning back to a harder glassy state (17, 18). Among the MB-stabilizing polymers available, we chose to employ poly(butyl cyanoacrylate, PBCA) because PBCA is extensively used, well characterized, and used in Food and Drug Administration-approved surgical superglue for wound closure (19).

## Significance

Microbubbles (MB) are widely used for ultrasound (US) imaging and US-mediated drug delivery. Thus far, only spherical MB have been employed, likely because surface tension thermodynamically forces air-filled bubbles to always exist in a perfect spherical shape. Here, we show that it is possible to generate nonspherical MB, applying thermal and mechanical energy to one-dimensionally stretch poly(butyl cyanoacrylate)–based polymeric MB. Nonspherical MB were found to move closer to blood vessel walls and have longer circulation times in vivo upon i.v. administration in mice. Because of this, upon combination with transcranial focused ultrasound, nonspherical MB outperformed spherical MB in temporarily permeabilizing the blood–brain barrier. These findings open up avenues for engineering nonspherical polymer-based MB for ultrasound-mediated drug delivery.

Author contributions: A.D., S.M., and T.L. conceived and coordinated the study; A.D., T.S., R.P., P.D., N.M., S.M., and T.L. designed research; A.D., T.S., R.P., E.R., Y.Z., C. Power, D.M., M.L., A.S., M.W., A. Motta, C. Porte, Z.M., A.S.E., R.B., A.G., A. McClelland, D.R., E.S., F.K., R.M.P., and L.D.L. performed research; A.D. and T.S. contributed new reagents/analytic tools; A.D., T.S., R.P., E.R., and A. Motta analyzed data; A.D. drafted the first version of the manuscript; T.S., S.M., and T.L. critically revised, corrected, and commented on the manuscript; and all authors read and approved the final version of the manuscript.

The authors declare no competing interest.

This article is a PNAS Direct Submission.



[1]A.D. and T.S. contributed equally to this work.

[2]To whom correspondence may be addressed. Email: mitragotri@seas.harvard.edu or tlammers@ukaachen.de.

This article contains supporting information online at https://www.pnas.org/lookup/suppl/doi:10.1073/pnas.2218847120/-/DCSupplemental.

Published March 20, 2023.

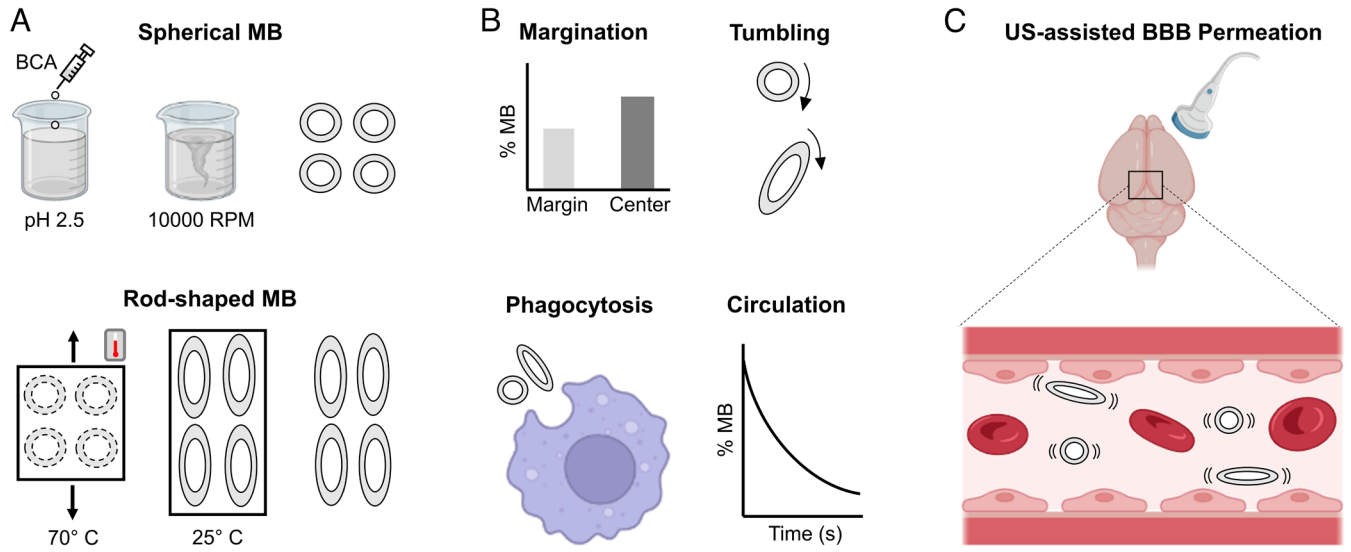


**Fig. 1.** Study setup. (*A*) Spherical MB were synthesized by anionic polymerization of butyl cyanoacrylate (BCA) in 1% (w/v) Triton™ X-100 at pH 2.5. Rod-shaped MB were generated by one-dimensionally stretching spherical MB at a temperature exceeding the glass transition temperature of PBCA, followed by cooling down to room temperature. (*B*) MB flow dynamics were studied by assessing their margination propensity, tumbling behavior, phagocytosis, and circulation kinetics. (*C*) Spherical and rod-shaped MB were intravenously administered, and their ability to permeate the BBB upon exposure to transcranial focused US was compared.

We generated rod-shaped MB by one-dimensionally stretching spherical PBCA MB above their glass transition temperature (Fig. 1*A*). We studied their flow dynamics by assessing margination propensity, tumbling motion, phagocytosis, and circulation kinetics (Fig. 1*B*). Finally, we evaluated their ability to permeate the blood–brain barrier (BBB) upon transcranial focused US treatment (Fig. 1*C*). Our findings show that tailoring the shape of MB modulates their flow dynamics and sonopermeation performance, and they thereby open up avenues for the use of anisotropic materials in US imaging and drug delivery.

## Results

**Generation of Anisotropic Microbubbles.** Spherical PBCA MB were prepared via anionic polymerization of BCA. To obtain rod-shaped polymeric MB, we adapted film-stretching technology which was previously employed for producing anisotropic polymeric nanoparticles (17, 18). Rod-shaped MB were generated by embedding the spherical PBCA MB in a poly(vinyl alcohol) (PVA) film, followed by heating the dried film above the glass transition temperature of PBCA, and subsequent mechanical stretching of the film in one direction. Since MB are prone to collapse during the drying, heating, and stretching procedures, we systematically optimized experimental conditions such as PVA solubility, PVA concentration, temperature, and the extent of mechanical stretching (*SI Appendix*, Table S1). We found that a high concentration of water-soluble PVA, a low temperature, and a low degree of mechanical stretching were optimal in generating intact rod-shaped MB.

Following successful fabrication of rod-shaped MB, we assessed their morphological and physicochemical characteristics (Fig. 2). Using three different microscopic imaging techniques, i.e., bright-field microscopy, cryogenic scanning electron microscopy (Cryo-SEM), and three-dimensional (3D) confocal laser scanning microscopy (CLSM), we confirmed the anisotropic shape of the MB (Fig. 2 *A–D*). We also demonstrated that they are hollow (Fig. 2 *C* and *D*) and air-filled, causing them to float due to buoyancy (as evidenced by the white MB cake in Fig. 2*E*). We furthermore characterized the rod-shaped MB with respect to their size, aspect ratio, surface area, shell thickness, and charge (Fig. 2*F*). As expected, for the rod-shaped MB, the lengths of the major and minor axes were significantly larger and smaller than the diameter of the spherical MB, respectively, resulting in the formation of MB with a significant increase in the aspect ratio and surface area. The size distribution of anisotropic and spherical MB was found to be similar (*SI Appendix*, Fig. S1). We validated that the MB retain their shape over time. We noted that rod-shaped MB retain their anisotropic shape in aqueous dispersion even after 7 d at 4° and 25 °C (*SI Appendix*, Fig. S2 *A–D*). Furthermore, at 37 °C, rod-shaped MB preserved their anisotropic shape for up to 1 h, thus indicating that they will retain their shape upon i.v. administration in vivo (*SI Appendix*, Fig. S2 *E* and *F*).

Next, we studied the US imaging properties and cavitation response of anisotropic rod-shaped MB. For the former, we embedded the MB in tissue-mimicking gelatin phantoms and exposed them to low–mechanical index (MI) US of 0.03 and 0.07. Qualitative and quantitative analysis revealed that anisotropic MB generated sufficient US contrast to be clearly detectable in both brightness mode and contrast mode, but they were less echogenic than their spherical counterparts (Fig. 2 *G* and *H*). We also compared the US contrast of spherical and anisotropic polymer-based MB to a clinical formulation SonoVue®. At preclinically relevant US frequencies, i.e., 18 MHz, we observed that both spherical and nonspherical PBCA MB generated stronger brightness-mode and contrast-mode signals than SonoVue ($P < 0.01$; *SI Appendix*, Fig. S3*A*). Conversely, at a clinical US frequency of 5 MHz, SonoVue® exhibited higher-contrast-mode US signals than PBCA MB ($P < 0.0001$; *SI Appendix*, Fig. S3*B*). To study MB cavitation response, they were exposed to high-MI US of 0.7. We confirmed good responsiveness to high-MI US by demonstrating that rod-shaped MB can be efficiently destroyed at the US settings used (*SI Appendix*, Fig. S4). We finally recorded the passive cavitation detection (PCD) signals of anisotropic and spherical MB. Both harmonic and broadband emissions (which represent stable and inertial cavitation, respectively) were detected, and their signal intensities were found to increase with increasing acoustic pressure (Fig. 2*I*). In comparison to spherical MB, anisotropic MB produced lower levels of harmonic and broadband signals (Fig. 2*I*). Together, these findings demonstrate that rod-shaped MB with an aspect ratio up to ~2.5 can be stably engineered via one-dimensional stretching

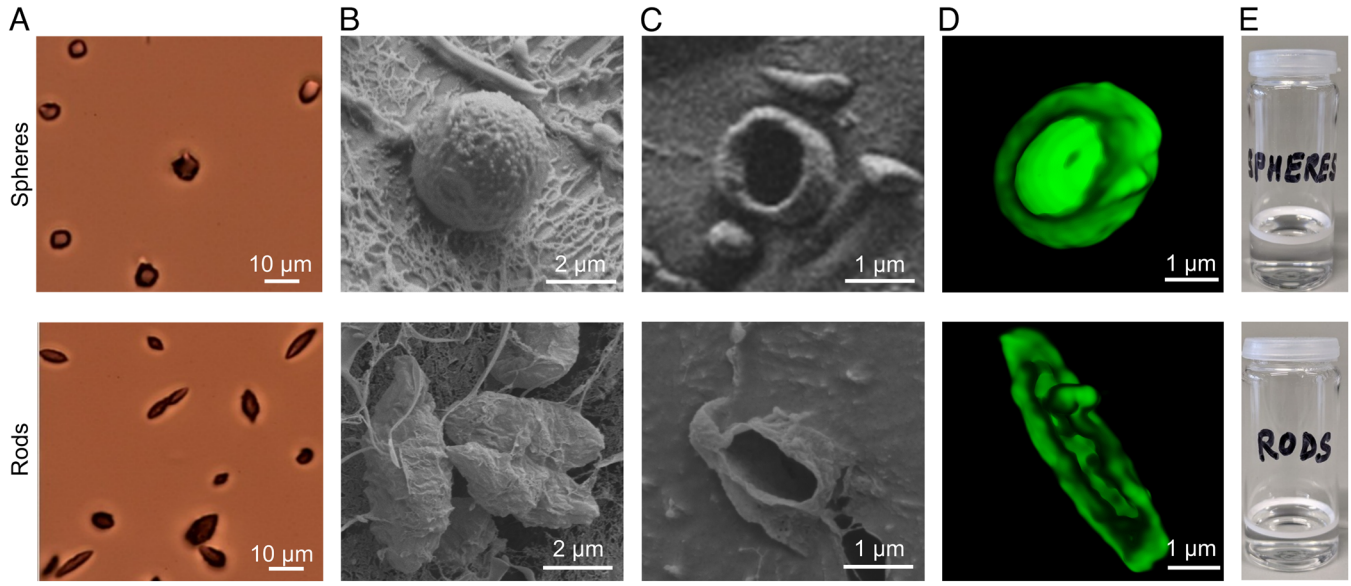


F

| Shape | Size (µm) | Aspect ratio | Surface area (µm$^2$) | Shell thickness (nm) | Charge (mV) |
|---|---|---|---|---|---|
| Spheres | 3.6 ± 0.1 | 1.1 ± 0.0 | 43.9 ± 2.3 | 233.8 ± 11.3 | -24.5 ± 0.1 |
| Rods | 7.3 ± 0.3 $^{\#}$<br>2.9 ± 0.2 $^{\#\#}$ | 2.6 ± 0.2 | 56.2 ± 3.0 | 200.3 ± 8.1 | -26.6 ± 1.0 |
| P-value | < 0.01 | < 0.0001 | < 0.01 | < 0.05 | < 0.05 |

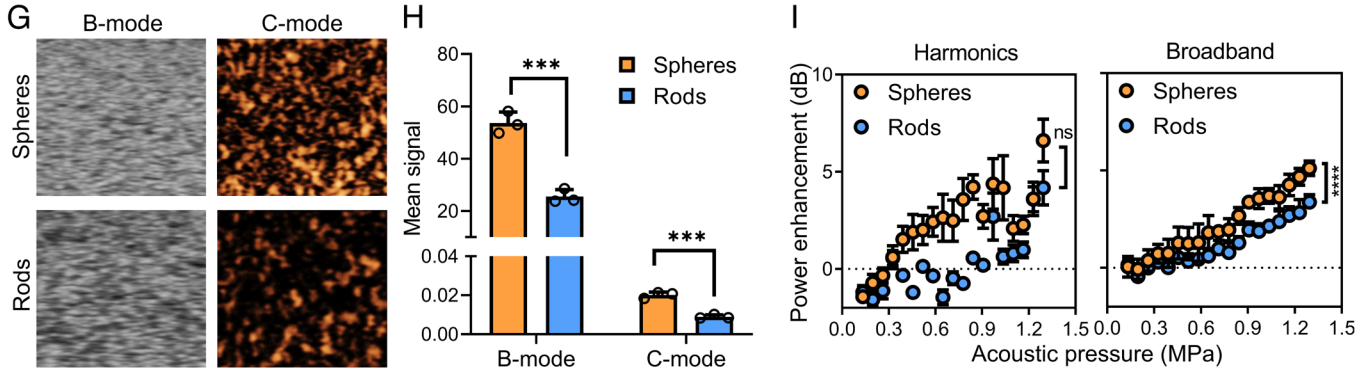


**Fig. 2.** Generation and characterization of anisotropic MB. (*A*) Bright-field, (*B* and *C*) cryogenic scanning electron, and (*D*) 3D confocal laser scanning microscopy of spherical and rod-shaped MB. (*E*) Both spherical and anisotropic rod-shaped MB float in aqueous dispersions due to buoyancy. (*F*) Physicochemical characteristics of spherical and rod-shaped MB. $^{\#}$ and $^{\#\#}$ represent the major and minor axis, respectively. (*G* and *H*) US imaging at 18 MHz center frequency and 0.03 mechanical index revealed that anisotropic MB produce less intense brightness-mode (B-mode) and contrast-mode (C-mode) US signals as compared to spherical MB. (*I*) Cavitation response analysis demonstrating that anisotropic MB emit lower levels of harmonic and broadband signals. Data represent mean ± SD of n = 3 independent MB batches. Statistical comparison between spheres and rods in panel *F* was performed using the unpaired Student *t* test. In panels *H* and *I*, unpaired *t* tests for multiple groups were used. ***$P < 0.001$ and ****$P < 0.0001$.

of spherical PBCA MB and that the resulting anisotropic MB exhibit US contrast and cavitation properties, although a factor of ~2 lower than spherical MB.

**Anisotropic Microbubbles Exhibit Enhanced Margination and Tumbling.** We hypothesized that upon intravenous (i.v.) administration, anisotropy would promote MB margination, i.e., their propensity to flow closer to the walls of blood vessels. We therefore initially studied the distribution of rod-shaped vs. spherical MB in a model microfluidic blood vessel under realistic flow conditions. We employed a straight-channel microfluidic chip and divided it into different regions depending on the distance of the MB to the channel walls: margin, intermediate, and center (Fig. 3*A*). We defined the margin as the channel width equivalent to the largest dimension of the MB (i.e., 7.3 µm); the remaining channel widths were equidistantly divided into intermediate and center regions. Coumarin-labeled MB were prepared as in ref. 20 (*SI Appendix*, Fig. S5) and used to visualize and quantify the distribution of anisotropic vs. spherical MB in the different regions of the channel at physiological flow rates and in the presence of erythrocytes.

Upon injection in microfluidic flow channels, we found that rod-shaped MB marginated more toward the margins of the channels, while spherical MB were more prominently present in the central region (Fig. 3*B*). When quantifying, we noted that the amount of anisotropic MB in the margin area was more than

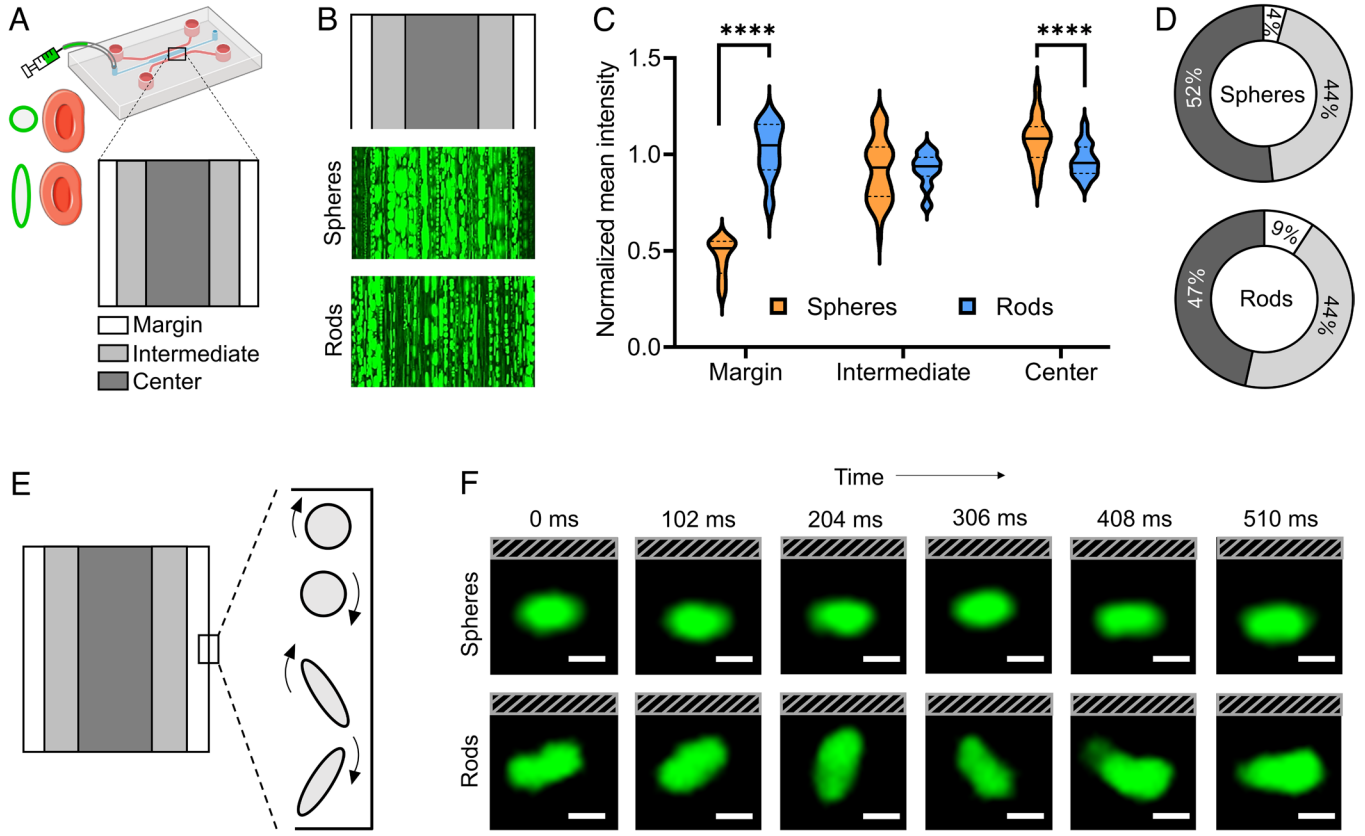


**Fig. 3.** Anisotropic MB demonstrate increased margination and tumbling. (*A*) Coumarin 6–labeled spherical and rod-shaped MB were injected into a microfluidic channel in the presence of red blood cells (16% hematocrit). Margination was assessed by analyzing MB distribution at physiological flow conditions in the margin, intermediate, and central zones of the channel. (*B*) Fluorescence microscopy images exemplifying that anisotropic MB flow more toward the marginal zones than spherical MB. (*C* and *D*) Quantification of MB distribution in the microfluidic channels showing that the percentage of rod-shaped MB flowing in the marginal zones of the microfluidic channel was more than twofold higher than that for spherical MB. (*E* and *F*) Schematic and time-lapse fluorescence microscopy analysis of the tumbling motion of spherical and anisotropic MB, illustrating tumbling of the latter near the channel wall (gray lines). (Scale bar, 1 μm.) Statistical comparisons were performed using unpaired *t* tests for multiple groups. ****$P < 0.0001$.

twofold higher than that for spherical MB (Fig. 3 *C* and *D*; $P < 0.000001$). In the margin area close to the vessel wall, we also recorded MB movement and orientation over time to study their tumbling motion (Fig. 3*E*). As expected, for spherical MB, hardly any tumbling could be observed (Movie S1). Conversely, for anisotropic MB, we did clearly detect tumbling events (Movie S2). Fig. 3*F* shows still images of these events for both MB formats, exemplifying that anisotropic shape promotes tumbling near the walls.

**Anisotropic Shape Reduces Microbubble Phagocytosis.** Upon i.v. administration, MB are very rapidly cleared from systemic circulation, typically within minutes (21). This rapid clearance is mainly mediated by macrophages in organs of the reticuloendothelial systems. Taking into account that several nanoparticle studies have shown that an anisotropic shape reduces (the kinetics of) macrophage clearance, we compared phagocyte uptake of anisotropic and spherical MB. To this end, we first incubated J774A.1 murine macrophages with coumarin 6–labeled spherical and rod-shaped MB. We next used the standard 4% paraformaldehyde fixation procedure to destroy and wash away the noninternalized MB (i.e., surface-bound and free-floating MB; *SI Appendix*, Fig. S6), and we then visualized and quantified the MB internalized at different time points. We observed that at early incubation times (i.e., 1 min), the rod-shaped MB displayed approximately threefold lower macrophage uptake as compared to spherical MB; however, these differences were not statistically significant (Fig. 4 *A* and *B*). At later incubation time points (i.e., at 10 min), the differences between both MB shapes became more prominent and statistically significant, with more than a 40-fold lower uptake observed for the rod-shaped MB compared to the spherical ones ($P < 0.05$; Fig. 4 *C* and *D*).

**Anisotropic Shape Prolongs Microbubble Circulation Time.** We next evaluated the in vivo circulation kinetics of anisotropic vs. spherical polymer-based MB. To differentiate gas dissolution from actual MB clearance, we first studied the preservation of US contrast over time under in vivo–like conditions. Upon incubating the MB at 37 °C, we did not observe changes in US contrast of spherical and anisotropic MB over time (*SI Appendix*, Fig. S7). Upon applying continuous US to MB during extended imaging, we found that their contrast gradually decayed and that anisotropic and spherical MB exhibited a similar decay (*SI Appendix*, Fig. S8).

Since anisotropic MB showed reduced macrophage uptake, we hypothesized that the kinetics of their in vivo clearance from the blood stream will be slowed. To study MB circulation kinetics, we administered them intravenously, and we used contrast-enhanced ultrasound (CEUS) to monitor circulating MB in the aorta of mice. Time-lapse CEUS showed that the blood contrast of anisotropic MB diminished less slowly than that for spherical MB (Fig. 5*A* and Movies S3 and S4). Representative time curves of MB blood circulation in the aorta are shown in Fig. 5*B*, which confirm the longer blood circulation time of the anisotropic MB compared to the spherical ones. On the basis of n = 5 animals per group, we finally determined key pharmacokinetic parameters, which demonstrated that anisotropic MB exhibited a slower

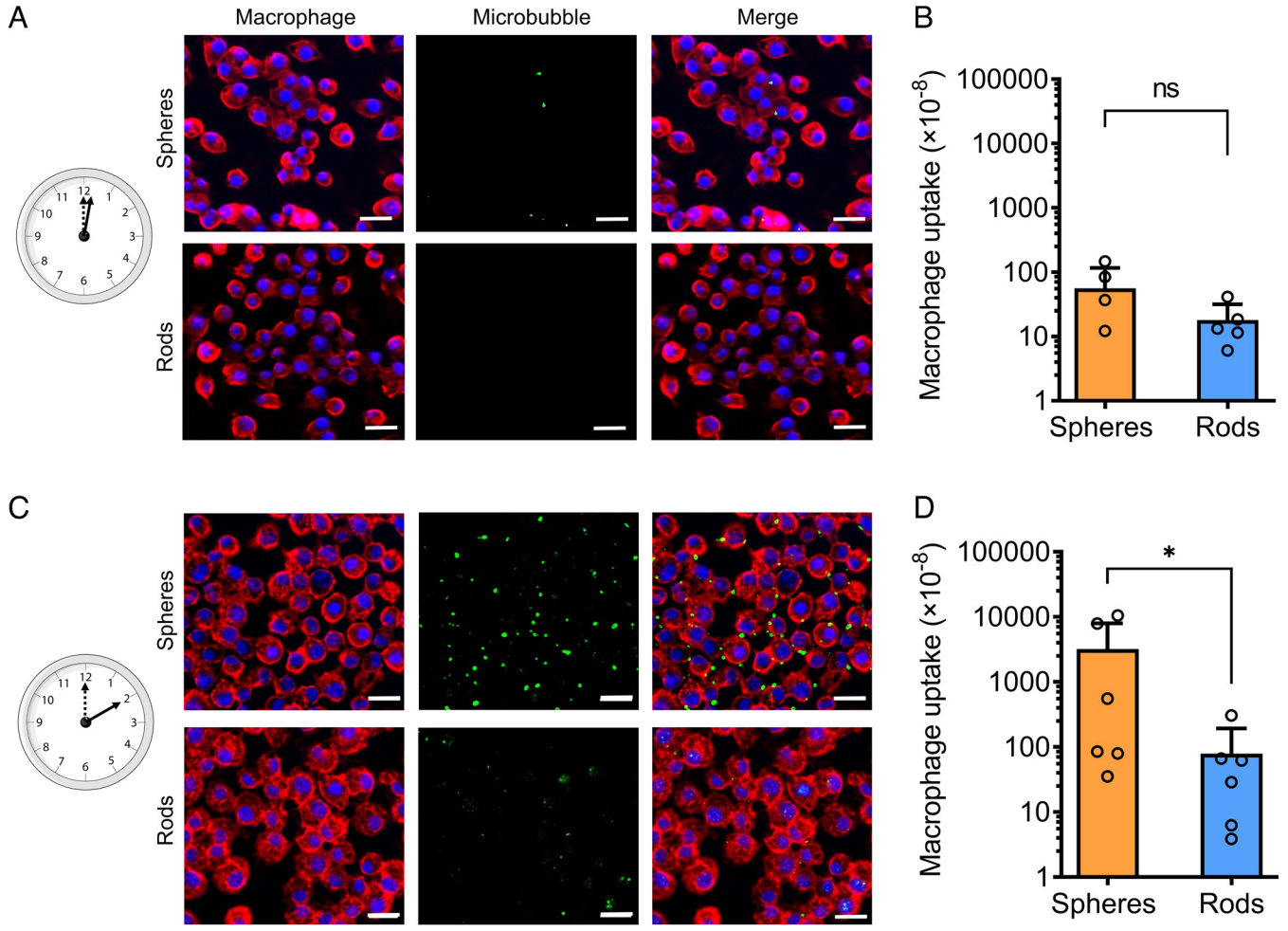


**Fig. 4.** Anisotropic shape reduces MB phagocytosis. J774A.1 murine macrophages were incubated with coumarin-labeled spherical and rod-shaped MB, and phagocytic uptake was analyzed. (*A–D*) At 1 and 10 min after the initiation of incubation, rod-shaped MB showed less macrophage uptake as compared to spherical MB. Cell nuclei and cellular membranes were stained with DAPI (blue) and wheat germ agglutinin (red), respectively. (Scale bar, 20 μm.) Data represent mean ± SD. Statistical comparisons were performed using the unpaired Student *t* test. *$P < 0.05$.

elimination rate ($P < 0.05$; Fig. 5*C*), increased area under the curve (AUC) (Fig. 5*D*), and prolonged blood half-life ($P < 0.05$; Fig. 5*E*) as compared to spherical MB.

**Anisotropic Microbubbles Potentiate Focused Ultrasound (FUS)–Induced Blood–Brain Barrier Permeation.** We finally evaluated if the enhanced margination, reduced phagocytosis, and the prolonged blood circulation of anisotropic MB can improve their in vivo sonopermeation performance. To this end, we evaluated BBB opening upon combining focused ultrasound (FUS) treatment with spherical and anisotropic MB.

Upon i.v. administration and FUS application, we first assessed the cavitation spectra of spherical and anisotropic MB in the mouse brain. We identified strong subharmonic, fundamental, and harmonic emissions with increasing acoustic pressures (*SI Appendix*, Fig. S9). As spherical and anisotropic MB showed slightly different cavitation properties in vivo, we performed a pulse ramping study to determine their individual cavitation thresholds (*SI Appendix*, Fig. S10). We noted that at these specific acoustic pressures, spherical and anisotropic MB produced equal levels of cavitation signals in vivo (*SI Appendix*, Fig. S10). Accordingly, we employed these acoustic pressure settings when performing the FUS-mediated BBB opening experiments.

We coadministered the model drug trypan blue together with either anisotropic or spherical MB, and upon subsequently applying transcranial FUS to induce localized BBB permeation, the brains of mice were harvested 1 h later to assess the extent of BBB permeation (Fig. 6*A*). During FUS application, we recorded the passive cavitation detection (PCD) signals of the MB to confirm that anisotropic and spherical MB produced similar levels of harmonic and broadband emission signals (Fig. 6 *B* and *C*). The cavitation behavior of anisotropic and spherical MB did cause some tissue damage in the sonicated brain region, as evidenced by erythrocyte extravasation and microhemorrhages (*SI Appendix*, Fig. S11). To assess if the improved margination and circulation behavior of rod-shaped MB translates into improved BBB permeability, trypan blue accumulation was assessed in the sonicated brain region (Fig. 6*D*). As shown in Fig. 6 *E* and *F*, anisotropic MB substantially promoted BBB permeation, resulting in an almost doubling of fluorescent model drug delivery into brain tissue (1,730.45 ± 1,077.76 vs. 966.70 ± 565.48; $P < 0.05$). We finally assessed the relationship between the acoustic emission signals and BBB permeation for both anisotropic and spherical MB. As shown in Fig. 6*H*, for anisotropic MB, BBB permeation showed a strong positive correlation to broadband emission signals (r = 0.71), while spherical MB displayed a weak positive correlation (r = 0.24). Overall, in the case of anisotropic MB, BBB permeation was found to be significantly correlated to both harmonic and broadband emission signals ($P < 0.05$), which is in contrast to spherical MB (Fig. 6 *G* and *H*). These findings showcase the significance of

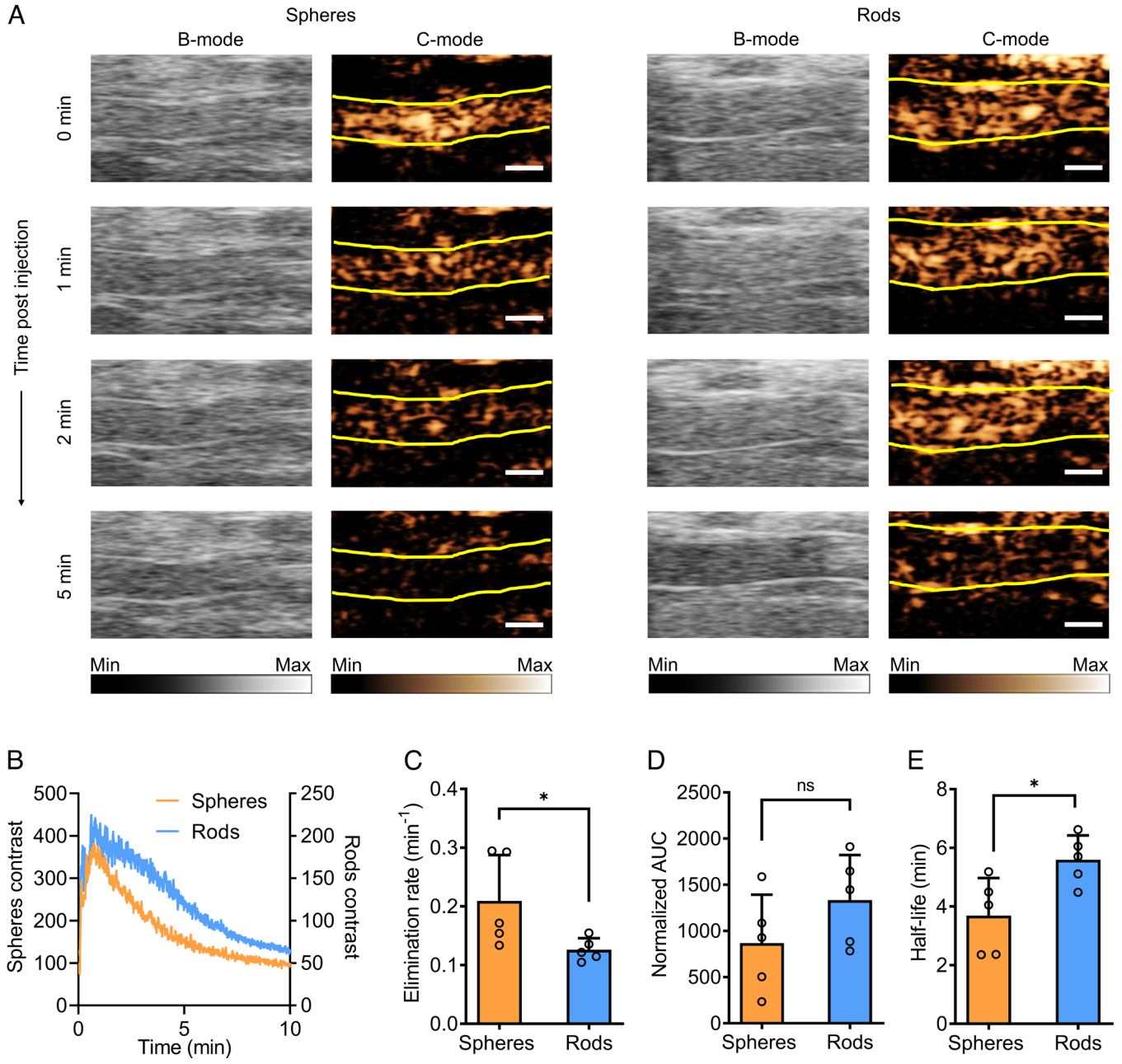


**Fig. 5.** Anisotropic MB display prolonged in vivo circulation times. (*A*) Time-lapse B-mode and C-mode US images at 18 MHz center frequency and 0.07 mechanical index, exemplifying that the US contrast of rod-shaped MB in the aorta decreases slower than that of spherical MB. Vessel borders outlined in yellow. (*B*) Continuous CEUS monitoring of MB signal up until 10 min after i.v. administration demonstrates prolonged circulation kinetics for anisotropic vs. spherical MB. (*C–E*) Pharmacokinetic analysis of elimination rate, area under the curve (AUC), and circulation half-life for spherical vs. rod-shaped MB. (Scale bar, 1 mm.) Data represent mean ± SD (n = 5). Statistical comparison is based on an unpaired Student *t* test. *$P < 0.05$.

anisotropic shape as a MB design parameter to assist in improving BBB permeation and (model) drug delivery to the brain.

## Discussion

We generated nonspherical polymer-based MB and investigated the impact of anisotropic shape on MB flow dynamics and sonopermeation performance. Our results show that nonspherical MB outperform traditional spherical MB, presenting with enhanced margination propensity, reduced phagocytosis, prolonged in vivo circulation time, and enhanced BBB permeation. These findings provide insights on the impact of MB shape on in vivo performance, and they open up avenues for US imaging and US-mediated drug delivery.

The generation of nonspherical MB is based on the glass transition property of the polymeric MB shell. Spherical PBCA MB were heated above their glass transition temperature of 56 °C to achieve a rubbery state (22), followed by a greater than twofold mechanical stretching of the MB in this soft rubbery state and subsequent gradual cooling of one-dimensionally stretched MB to temperatures below their glass transition temperature to eventually attain a more glassy solid state. Of note, all other preclinical and clinical MB formulations developed to date are spherical in shape (23–25). Our efforts therefore expand the MB design landscape by introducing anisotropic MB.

We studied the margination of anisotropic MB, i.e., the migration of MB toward the vessel wall. Several studies have described that spherical MB travel mostly in the center of blood vessels (26, 27).

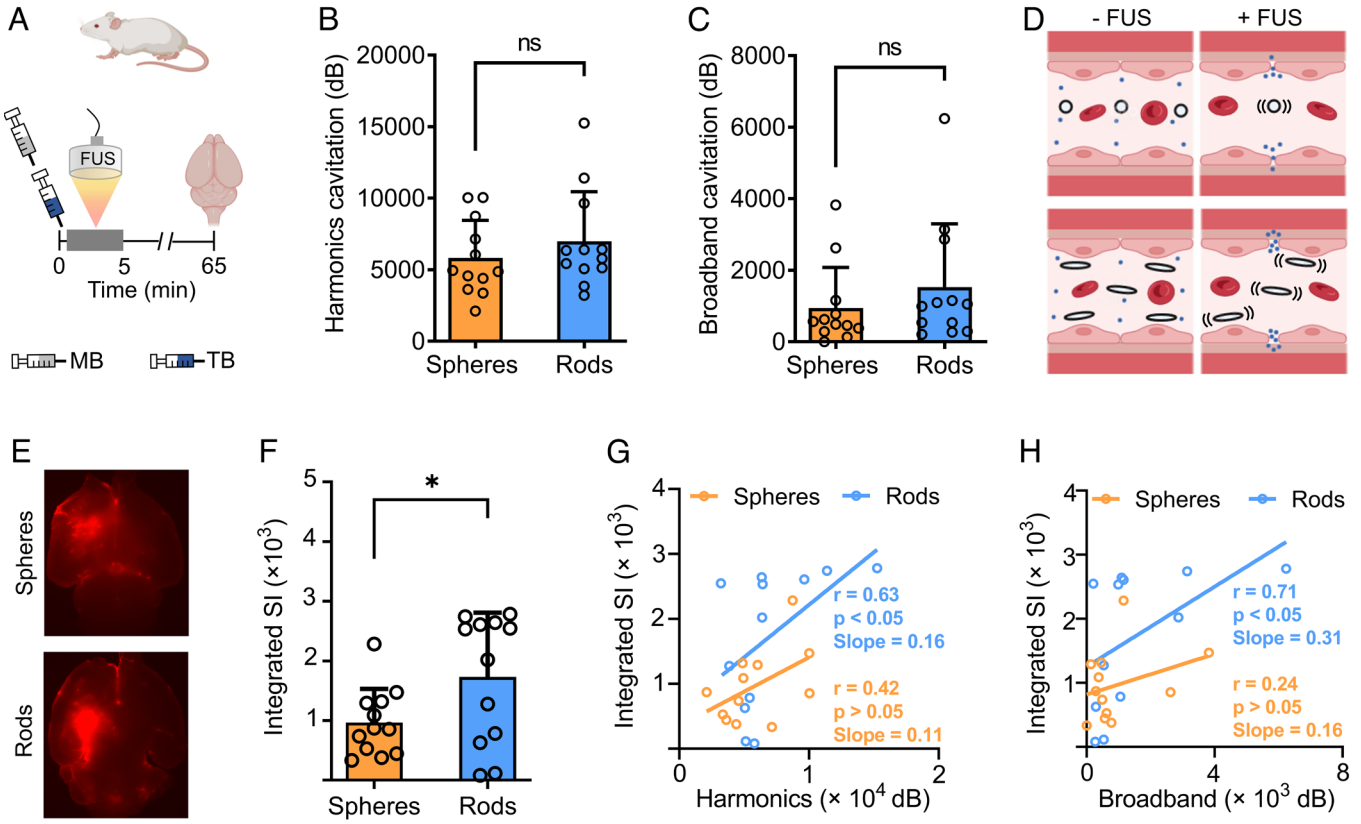


**Fig. 6.** Anisotropic MB potentiate FUS-induced BBB permeation. (*A*) BBB permeation was induced by administering $1 \times 10^9$ MB and transcranially applying FUS to the brain. Trypan blue was used as a fluorescent model drug to capture the extent of BBB permeation. (*B* and *C*) Quantification of harmonic and broadband US signals in the brain indicates that in our experimental setup, spherical and anisotropic MB produced similar levels of cavitation. (*D*) Schematic showing how the enhanced margination and prolonged circulation time of rod-shaped MB may contribute to enhanced BBB permeation. (*E* and *F*) Ex vivo fluorescence imaging of a brain section and quantification (in n = 12 mice per group) showing that anisotropic rod-shaped MB more efficiently promote BBB sonopermeation than spherical MB. (*G* and *H*) Correlation of BBB permeation with acoustic emission signals, exemplifying a higher positive correlation and slope for anisotropic vs. spherical MB. Data represent mean ± SD. Statistical comparisons for panels *B*, *C*, and *F* were performed using unpaired Student *t* tests, while in panels *G* and *H*, comparisons were analyzed using the Spearman correlation. *$P < 0.05$.

To enhance the margination of standard spherical MB, numerical simulations and experimental finding have shown that acoustic radiation forces can potentially be employed for this purpose, although quite difficult to control (26–28). The microfluidics results presented here exemplify that nonspherical polymeric MB intrinsically possess margination propensity at 16% hematocrit and at steady flow conditions. We chose this specific hematocrit level for analytical reasons because higher levels would interfere with the Light-emitting diode (LED) source and fluorescent signals. At higher hematocrit levels, e.g., 40% as in the circulation of healthy individuals, nonspherical MB are assumed to be colliding even more frequently with erythrocytes and thus to be undergoing even more lateral drifts and enhanced migration toward the vascular walls (29–31).

Our results also demonstrate tumbling motion of nonspherical MB close to the walls, where erythrocyte concentrations are typically relatively low. This indicates that the tumbling events are likely mostly due to MB shape effects and not bumping to erythrocytes (31, 32). We consequently expect that also under high hematocrit conditions, nonspherical MB will prominently tumble near the vessel walls. We furthermore believe that also under pulsatile (i.e., heart beat-dictated) flow conditions, the margination and tumbling propensity of nonspherical MB will be retained, as previous studies have shown that pulsatile flow does not negatively impact margination of nonspherical nano- and microparticles and cells (33–35). Since nonspherical MB will concentrate near vessel walls, they will also likely travel at reduced velocities in contrast to the MB in the center of the flow stream (27). Overall, these phenomena are assumed to be increasing both the contact and the interaction time of nonspherical MB with the endothelium, thus promoting molecular imaging, vessel permeation, and drug delivery.

Phagocytosis and circulation kinetics affect the in vivo performance of MB. In systemic circulation, nano- and microsized materials are covered with opsonins and cleared by phagocytic cells of the reticuloendothelial system (32). Previously, it has been shown that phagocytic activity can be reduced, and circulation time enhanced, by tailoring MB size, shell composition, and charge (36–40). We here extend these efforts by demonstrating that also the shape of MB affects phagocytic uptake and in vivo circulation time. The cellular mechanisms behind this shape-dependent phagocytosis of MB are thus far only partially understood. It has been previously demonstrated that the point of initial attachment between a macrophage and a nonspherical particle dictates phagocytosis (14). When a macrophage attaches along the pointed ends of a rod-shaped particle, the expansion of the actin ring required to surround the particle from all sides is relatively small, and thus, the particles can be effectively phagocytosed. Conversely, when a macrophage attaches along the flat sides of the rod-shaped particle, expansion of the actin ring necessary to surround the particle is high and requires substantial energy, thus reducing the likeliness of the particle to be phagocytosed (14). These notions may explain the reduced phagocytosis of nonspherical MB observed here. Our findings are furthermore in line with

reports showing reduced (i.e., frustrated) phagocytosis and prolonged circulation times for nonspherical vs. spherical nanoparticles (14, 15, 41). As our nonspherical MB show reduced phagocytic uptake rate and are more slowly cleared from systemic circulation, we expect that they will also accumulate less rapidly in RES organs in vivo (42–44), thereby endowing them with an expanded time window to be used for US-assisted drug delivery.

When MB are combined with US, they oscillate and generate shear forces, thereby promoting drug delivery across the vascular endothelium and cellular membranes (25, 45). This process is referred to as sonoporation or sonopermeation, and it has been widely explored to enhance drug delivery to tumors and to the brain (4–7). Several factors are known to affect the extent of BBB sonopermeation. Parameters, such as mechanical index, peak negative pressure, frequency, and pulse repetition frequency, are systematically optimized to enhance the sonopermeation effect (25). For MB, design features such as size, shell composition, and shell stiffness have been explored to promote BBB opening (46–48). Here, we show that the shape of MB, as a previously unexplored design parameter, significantly impacts the degree of BBB sonopermeation. This improvement likely results from the sum of enhanced margination, reduced phagocytosis, and prolonged in vivo circulation time of nonspherical MB.

Reflecting on the present results, there are multiple ways forward to further improve the performance and impact of anisotropic MB. First, hard-shell MB typically undergo destruction upon FUS treatment, which may result in vascular and tissue damage during BBB opening. This damage may be mitigated by engineering softer-shell polymeric MB, which may enable more controlled oscillation and/or destruction. Such softer-shell MB can be produced by tuning surfactant properties or by adding propylene glycol as a membrane softener (11, 49). Second, with our materials and methodology, we were only able to generate nonspherical MB with an aspect ratio of 2.5. To engineer nonspherical MB with a higher aspect ratio, it will be crucial to develop protocols that enable films to withstand higher degrees of mechanical stretching. This can be achieved by employing more durable materials for film production and by lowering the glass transition temperature of the polymeric MB, thus facilitating film stretching at reduced temperatures. Third, we here only studied rod-shaped MB. Follow-up studies could explore the performance of other nonspherical shapes, such as discs (mimicking the shape of erythrocytes for potentially even longer circulation) or stars (mimicking the shape of activated platelets for enhanced surface area expansion) (50, 51). These biomimicking nonspherical shapes may promote MB performance in various US imaging and drug delivery setups. Finally, to promote widespread use, the production methodology of anisotropic MB needs to be refined as our current fabrication protocol does not allow for automated and high-throughput production, thereby complicating large-scale manufacturing.

Taking together, we here discovered that anisotropic MB can be stably generated using polymer-based starting materials. Rod-shaped polymeric MB outperformed spherical MB by enhanced margination, reduced phagocytosis, improved circulation times, and increased BBB sonopermeation. Beyond sonopermeation and drug delivery, we postulate that rod-shaped MB may also be beneficial for molecular imaging purposes. For instance, in the case of large-sized and higher flow rate vessels (e.g., carotid arteries), the margination of rod-shaped MB will become increasingly more important to facilitate their binding to the activated endothelium. The findings presented here, together with other reported advances on rod-shaped gas vesicles (performed by Shapiro et al. and others), expand the landscape of nonspherical US-responsive agents (52–54). These nonspherical US-responsive materials hold significant potential for improving US imaging, US-enhanced drug delivery, and US-assisted therapeutic interventions.

## Materials and Methods

**Materials.** Butyl cyanoacrylate (BCA) was purchased from Special Polymer Ltd (Bulgaria). Cold water–soluble PVA (87 to 90% hydrolyzed and molecular weight 30,000 to 70,000 Da), coumarin 6, Triton™ X-100, gelatin, and dimethylsulfoxide (DMSO) were bought from Sigma-Aldrich (Germany). Glycerol was procured from VWR. Trypan blue was obtained from Thermo Fisher Scientific. J774A.1 cells were obtained from the American Type Culture Collection (ATCC, Manassas, Virginia, USA). Deionized (DI) water was used for all experiments, and all other reagents were of appropriate analytical grade.

**Synthesis of Spherical MB.** Spherical shaped poly(butyl cyanoacrylate) (PBCA) MB were synthesized using a previously established protocol (48). Briefly, 3 mL of BCA monomer was added dropwise to a 300 mL aqueous solution containing 1% (w/v) Triton™ X-100 at pH 2.5. Upon dropwise addition of BCA, the mixture was homogenized at 10,000 rpm for 1 h using an ULTRA-TURRAX (IKA-Werke, Germany). This led to the formation of spherical shaped PBCA MB. Subsequently, these MB were purified by multiple centrifugation steps at 500 rpm for 20 min and were finally suspended in 0.02% (w/v) Triton™ X-100 at pH 7.

**Synthesis of Rod-Shaped MB.** Rod-shaped PBCA MB were synthesized as per the previous particle-stretching protocol (17). Briefly, 15 g cold water–soluble PVA was dissolved in 80 mL of 0.02% (w/v) Triton™ X-100 at room temperature, followed by the addition of 1 mL of glycerol to reduce the glass transition temperature of PVA. We subsequently added 5 mL of spherical MB to the mixture under constant stirring, and the mixture was passed through a 100-μm cell strainer to remove the aggregates. The solution was then poured on a flat surface, and the film was allowed to dry for 24 to 48 h. The films were cut into 5- X 5-cm sections and mounted on a custom-built 1D stretcher with the aid of screws. The 1D stretcher was then placed in a paraffin oil bath at 70 °C for 10 min. Upon liquefaction, the films were stretched manually in one direction inside the oil bath and were subsequently allowed to cool down at room temperature for 30 min. In order to remove the residual oil, the films were cleaned with delicate task wipers (KimWipes) and isopropanol multiple times. The MB were extracted by dissolving the film in 0.02% (w/v) Triton™ X-100 at room temperature. Finally, the obtained rod-shaped MB were allowed to float due to buoyancy, and the underneath aqueous solution was replaced multiple times to remove precipitates and excess reagents.

**Synthesis of Coumarin-Labeled MB.** Coumarin-loaded spherical shaped MB were synthesized using a two-step strategy (20). In the first step, spherical MB were synthesized using the protocol as described above. In the second step, 50 mg of coumarin was dissolved in 1 mL DMSO and was subsequently mixed in 20 mL of an aqueous suspension containing $10^{11}$ spherical MB. The reaction was allowed to proceed for 24 h at room temperature. To remove the unloaded fluorophore, MB were allowed to float due to buoyancy, and the underneath aqueous solution was replaced multiple times until there was no unloaded fluorophore present. Finally, the coumarin-loaded spherical shaped MB were suspended in 0.02% (w/v) Triton™ X-100 at pH 7 and stored at room temperature until further use. To synthesize coumarin-loaded rod-shaped MB, we mechanically deformed the coumarin-loaded spherical MB by employing the same stretching procedure as described above.

**Beckman Coulter Counter.** The size distribution and concentration of PBCA MB were analyzed using a Multisizer 4 (Beckman Coulter, Germany) which was equipped with a 30-μm sensor orifice (48). Briefly, 20 mL of isotone solution was poured into a Coulter counter cup and was placed on the sample platform. This was used as a blank measurement in order to correct for background noise. Subsequently, 10 μL of PBCA MB was diluted with 20 mL of isotone solution, and the sample was measured in volumetric mode with a dilution factor of 2,000. These steps were repeated in triplicates to obtain mean ± SD.

**Bright-Field Microscopy.** To confirm the shape of the formed MB, we employed an Olympus BX41 microscope equipped with a microEye camera (Carl Zeiss, Oberkochen, Germany). We placed a drop of the sample on a HistoBond adhesive microscope slide (Paul Marienfeld GmbH & Co.KG, Lauda-Königshofen, Germany) and measured it in bright-field mode. The images were acquired using Olympus

50× LMPlanFL N objective. MB size was measured from bright-field images using ImageJ software. The aspect ratio and surface area were estimated from the two-dimensional (2D) projection images and mathematical equations for the respective shapes.

**Cryo-SEM.** Cryogenic scanning electron microscopy was used as a complementary imaging technique to confirm the shape and morphology of the formed MB. Measurements were obtained using a FE-SEM Zeiss Ultra 55 (Oberkochen, Germany) having a Leica VCT 100 Cryo stage and transfer shuttle. Spherical and rod-shaped MB were capped onto the sample holder and frozen in slush nitrogen. The sample holder was then inserted into the preparation chamber Leica Med 020 fitted with VCT 100 (Leica, Wetzlar, Germany) transfer shuttle. The MB droplets were fractured using a carbide knife, then sublimed at −100 °C for 5 min, and finally coated with 5 nm of 80:20 Pt/Pd. Readings were taken at 3 kV and 2 μA.

**CLSM.** Confocal laser scanning microscopy was used as a second imaging technique to confirm the shape of the MB. Coumarin-loaded spherical and rod-shaped MB were diluted with 1% agar solution (AppliChem, Darmstadt, Germany) in a 1:1 ratio. A single drop of this mixture was placed on the glass slide and covered with a coverslip (170 μm, No. 1.5H). A Leica TCS SP8 STED 3X microscope (Leica Microsystems, Germany) equipped with a plan apochromat 100×/1.40 oil immersion objective was used for visualizing the coumarin-loaded MB. The excitation wavelength was set at $\lambda = 470$ nm via a filtered white light laser, and the resulting emission was detected at $\lambda = 490$ to 550 nm using a HyD-SMD. Deconvolution of the images was processed using Scientific volume imaging (SVI) Huygens Professional software via the classic maximum likelihood estimation method.

**US Imaging of Spherical and Rod-Shaped MB.** We employed both preclinical (Vevo 2100, VisualSonics, Canada) and clinical US devices (Canon Medical Systems, Japan) to visualize the contrast generated from spherical and rod-shaped MB (11). For the preclinical US device, measurements were performed using a linear-array MX-250 transducer at 18 MHz center frequency. In case of the clinical US device, measurements were performed with a PLT 1005BT linear transducer connected to an Aplio 500 scanner at a frequency of 5 MHz. For sample preparations, $1 \times 10^8$ MB were diluted to 4.5 mL DI water, and the mixture was added into 10% (w/v) gelatin phantoms. The phantoms were imaged in both brightness mode (B-mode) and nonlinear contrast mode (C-mode) at mechanical indices of 0.03, 0.07, and 0.7. A region of interest was drawn at the center of all images, and the resulting contrast intensity was analyzed using Vevo LAB software. The US imaging contrast of spherical and rod-shaped MB was derived from the contrast intensity generated at 0.03 and 0.07 MI. Furthermore, the percentage of MB destruction was quantified as %MB destruction = [(contrast intensity at 0.03 MI–contrast intensity at 0.7 MI)/contrast intensity at 0.03 MI] × 100%.

**Design and Fabrication of Microfluidic Chip.** To study the margination propensity of spherical and rod-shaped MB, a custom-designed polydimethylsiloxane (PDMS) microfluidic device was used whose channel size was equivalent to that of large capillaries. The single channel microfluidic chip was fabricated using a previously established protocol (55). Briefly, a SU8–50 master was used as a mold for PDMS replicas of the chip. First, a 40-μm-thick layer of SU8–50 photoresist (Microchem) was spin coated on a silicon wafer (4 in.-P doped-⟨100⟩-10 to 20 $\Omega/cm^2$–525 μm thick from Si-Mat) at 2,000 rpm for 30 s. Next, the negative SU8–50 template was pre- and soft-baked for solvent evaporation, exposed to UV light, and baked again for epoxy cross-linking. This template was replicated using a mixture of PDMS and curing agent Sylgard 182 (Dow Corning Corporation) at a ratio of 10:1 (w/w). Specifically, the mixture was poured on the SU8–50 template, cured in an oven at 60 °C for 15 h, and moved at −20 °C for 1 h. After peeling off from the template, the channel extremities of the PDMS replica were punched via a biopsy puncher (OD = 1 mm, Miltex) to form inlet and outlet ports. Finally, upon oxygen plasma treatment (pressure = 0.5 mBar, power = 15 W, and time = 15 s; Plasma System Tucano, Gambetti), PDMS replica was sealed with a glass slide (20 × 60 × 0.17 mm) (no. 1.5H, Deckaläser). The resulting microfluidic chip has a rectangular cross-section with a width w = 210 μm, height h = 42 μm, and a port-to-port length l = 2.7 cm.

**Margination Analysis.** The margination analyses were run using an epifluorescence inverted microscope (Leica 6000; Leica Microsystems, Germany). Spherical and rod-shaped MB were diluted to obtain a suspension containing $6 \times 10^7$ MB/mL. The dilutions were performed in PBS with calcium and magnesium (Merck–Sigma, Germany) either in the presence or absence of 40% freshly harvested rat blood (hematocrit = 16%). Rat blood was collected into a heparin tube by heart puncture and later the animals were killed. A 1-mL syringe was loaded with the MB suspension and connected to a polyethylene tube guiding the flow to the inlet of the microfluidic chip. Another tube was connected to the channel outlet and placed into a waste collector. The channel was initially filled with the diluent medium; then, the flow was started at 100 nL/min. Three different chips were used for each experimental point, and each chip was imaged in three different areas in order to minimize possible flow variation. Movies were acquired as soon as the flow became stable. A total of 30 movies, with a duration range of 30 to 50 s, were acquired for each experimental point. To run the margination analysis, all the frames of each movie were merged to highlight MB position over time, generating a series of time projection images (TPIs) (LasX software; Leica Microsystems, Germany). A plot profile was then generated for each TPI by using ImageJ (NIH–USA). The plot profile of half the channel was then represented on a polar graph. The channel area was segmented into 3 macro areas: margin, intermediate, and center, and each area was composed of left and right sections. Considering the symmetry of the channels, each of the analysis was conducted in both the halves of each TPI. For the generation of the merged images, representative TPIs were merged together and false colored by using the Lookup Table: Fire from ImageJ software.

**Cell Culture.** J774A.1 murine macrophages were obtained from the American Type Culture Collection (ATCC, Manassas, Virginia, USA) and maintained in Dulbecco's modified eagle's medium (DMEM)–low glucose with 10% fetal bovine serum and 1% penicillin/streptomycin. Cells were passaged every 3 d in T75 flasks. After the cells reached confluency, $5 \times 10^5$ J774A.1 cells in DMEM were seeded on 12-mm-round coverslips in a 24-well plate at 37 °C. Once the cells adhered to the coverslips and reached 80% confluency, they were employed to study the uptake of spherical and rod-shaped MB.

**In Vitro Macrophage Uptake of Spherical and Rod-Shaped MB.** First, $2 \times 10^7$ coumarin-labeled MB was incubated with the adhered J774A.1 cells for 1, 5, and 10 min at 37 °C. Upon incubation, the samples were then washed with PBS, fixed with 4% paraformaldehyde for 10 min, and again washed with PBS at room temperature. To stain the cell membrane and nucleus, samples were incubated with wheat germ agglutinin (1:500) Alexa Fluor 594 (ThermoFisher Scientific, Massachusetts, USA) and DAPI (1:500) (ThermoFisher Scientific, Massachusetts, USA), respectively, at room temperature for 30 min. Subsequently, the samples were washed with PBS several times, and the 12-mm round coverslips used as cell supports were removed from the 24-well plates using surgical tweezers. Finally, a drop of Mowiol mounting medium was placed on each HistoBond adhesive microscope slide (Paul Marienfeld GmbH & Co.KG, Lauda-Königshofen, Germany) for adhering and attaching the coverslips.

**Fluorescence Microscopy.** To analyze the macrophage uptake of MB, images were acquired using an Axio Imager M2 fluorescence microscope equipped with an AxioCam MRm Rev.3 camera (Carl Zeiss Microscopy GmbH, Oberkochen, Germany). These images were acquired at magnifications of 100× and 400× using the channels DsRed (for cell membrane), GFP (for MB), and DAPI (for nucleus). Next, all raw image files were imported to Fiji software (ImageJ, NIH) via Bio-Formats plugin. A custom macro script was applied to automatically detect MB, maintaining a constant windowing and thresholding level and colocalizing MB fluorescent signal with a region of interest extracted from macrophages signal. Finally, macrophage uptake was quantified and was defined as the fraction of area colocalized by the MB signal to the area covered by the macrophages.

**Animal Experiments.** All animal procedures were performed using protocols approved by the German State Office of Nature, Environment and Consumer Protection (LANUV) North Rhine-Westphalia and by the Institutional Animal Care and Use Committee at Brigham and Women's Hospital. In these studies, all injections were administered intravenously into the lateral tail vein unless stated otherwise.

**Circulation Kinetics Analysis.** To study the circulation kinetics, a preclinical US device (Vevo 2100, VisualSonics, Canada) was employed to visualize the MB contrast as a function of time in the aorta. Ten 6- to 8-wk-old female BALB/c nude mice were obtained from Janvier Labs. Mice were randomly divided into 2 groups

with 5 animals each. The first one was administered with spherical MB, while the second one received rod-shaped MB.

Intravenous probe injection and noninvasive US imaging were performed on a temperature-controlled base to ensure maintenance of the animals' body temperature (36.9 °C ± 1 °C) under inhalation anesthesia (induction with 4 vol.% isoflurane with flow rate 1.8 L/min in oxygen-enriched air in an induction chamber and maintenance of anesthesia with 2 vol.% isoflurane with flow rate 1.2 L/min in oxygen-enriched air) using a dedicated vaporizer. Eyes were protected from desiccation using Bepanthen ointment. Mice were placed below the MS250 transducer at 18 MHz center frequency. Prior to MB injection, B-mode and pulsed-wave Doppler mode were employed to analyze the vessel edges and blood velocity, respectively, in the aorta (56). This standard procedure enabled precise positioning of the US transducer on the aorta. Subsequently, $10^9$ MB were injected, and amplitude modulation–based nonlinear contrast mode was continuously employed for 10 min at a mechanical index of 0.07. Using Vevo LAB software, a region of interest was drawn within the walls of the aorta, and the resulting US contrast intensity was analyzed as a function of time. Finally, the time-dependent US curves were then fit to a single-phase exponential decay curve, and pharmacokinetics parameters such as elimination rate, area under the curve (AUC), and blood half-lives were derived.

**FUS-Mediated BBB Permeation.** BALB/c mice that were 6- to 8-wk-old were anesthetized by i.p. injections of ketamine (80 mL/kg/h) and xylazine (10 mL/kg/h). After anesthesia, the fur on the head was removed using clippers and depilatory cream for efficient US propagation. The head was fixed in an acrylic stereotactic frame, and then, the mouse was placed on the FUS device.

Mice were randomly divided into 2 groups with 12 mice each. The first group received spherical MB, while the second one was administered with rod-shaped MB. To determine the acoustic pressures for the FUS-mediated BBB opening, we first assessed the in vivo cavitation threshold of spherical and rod-shaped MB by performing pulse ramping study. Based on this study, we chose 0.91 MPa and 1.29 MPa as the inertial cavitation thresholds for spherical and rod-shaped MB, respectively. This ensured that both spherical and rod-shaped MB produced similar levels of cavitation emission in vivo. For FUS-induced BBB opening, mice first received a dose of trypan blue, followed by the administration of $10^9$ MB. Immediately after the injections, FUS was applied to induce BBB permeation. FUS was applied using 10-ms bursts at 4 Hz for 100 s. The sonications were applied on four targets in a 2 × 2 grid pattern centered in the brain striatum to permeate the BBB. A FUS system with cavitation-controlled transmission was designed and built in-house. An air-backed, spherically curved lead zirconate titanate transducer (diameter/radius of curvature: 10/8 cm) was used for FUS transmission with a resonant frequency of 278 kHz. Sonications were applied at the third harmonic of the transducer (835 kHz) in order to decrease the focal spots for small animal experiments. The transducer was mounted on a plastic plate which was attached to a manually operated, three-axis positioning system. The transducer was driven by a function generator (33220A, Agilent, Santa Clara, CA, USA) and an amplifier (240L, E&I, Rochester, NY, USA). Electrical power output was measured using a power meter (E4419B, Agilent, Santa Clara, CA, USA) and a dual-directional coupler (C5948-10, Werlatone, Patterson, NY, USA). Transducers were calibrated using scans of the focal plane acquired with a needle hydrophone (HNC-1000; Onda, Sunnyvale, CA) and radiation force balance measurements to estimate the pressure amplitude at the focus in water. The width and length of the 50% isopressure contours were 1.9 and 11.4 mm, respectively. Pressure amplitudes presented here are those estimated in water without considering the skull insertion loss.

PCD recordings were performed using detectors with a resonant frequency of 650 kHz. The window for calculating broadband noise was also centered around 650 KHz for high sensitivity (the whole window length is 20,000 samples, with a sampling frequency of 10 MHz). The cavitation signal was recorded using a 12-bit high-speed digitizing card (PCX-5124, National Instruments, Austin, TX, USA). The time signal, frequency spectrum, and the tracked harmonic and wideband emissions were monitored and controlled in real time using in-house developed software in MATLAB (MathWorks, Natick, MA, USA).

**Ex Vivo Fluorescence Brain Imaging.** BBB permeation was assessed by imaging the accumulation of trypan blue in the brain. Therefore, brains were first harvested upon transcardiac perfusion 1 h after the FUS treatment. All the harvested brains were fixed with 4% paraformaldehyde, followed by serial sectioning from the dorsal surface to the ventral surface with a thickness of 1 mm. To visualize the accumulation of trypan blue, fluorescent images of the brain sections were acquired using a fluorescence stereo zoom microscope (ZEISS Axio Zoom.V16, Carl Zeiss AG, Oberkochen, Germany). Finally, the accumulation of trypan blue in the brain was quantified by measuring the total fluorescence intensity of all the brain sections for each mouse.

**Statistical Analysis.** Data are represented as mean ± SD. All results were analyzed using GraphPad Prism 9.1.1. Statistical analysis was performed using an unpaired *t* test for multiple groups by the two-stage step-up method (Benjamini, Krieger, and Yekutieli), unpaired Student *t* test, or Spearman r correlation as indicated in figure legends. Significance was determined at the following cutoff points: $*P < 0.05$, $**P < 0.01$, $***P < 0.001$, and $****P < 0.0001$.

**Data, Materials, and Software Availability.** All study data are included in the article and/or *SI Appendix*.

**ACKNOWLEDGMENTS.** T.L. acknowledges support by the European Commission (EuroNanoMed-III: NSC4DIPG), the European Research Council (ERC-CoG 864121: Meta-Targeting), and the German Research Foundation [Deutsche Forschungsgemeinschaft: GRK/RTG2375 (grant #331065168) and SFB 1066]. N.M. acknowledges support from the NIH (R01 EB033307). P.D. acknowledges the Clean Room and Microscopy Facilities at the Italian Institute of Technology in Genoa. S.M. acknowledges support from the Harvard John A. Paulson School of Engineering and Applied Sciences at the Harvard University. This work was performed in part at the Harvard University Center for Nanoscale Systems, a member of the National Nanotechnology Coordinated Infrastructure Network, which is supported by the NSF under NSF award no. ECCS-2025158. We acknowledge the use of https://biorender.com/ for creating schematics.

Author affiliations: [a]Institute for Experimental Molecular Imaging, Medical Faculty, Rheinisch-Westfälische Technische Hochschule Aachen University, 52074 Aachen, Germany; [b]John A. Paulson School of Engineering and Applied Sciences, Harvard University, Cambridge, MA 02138; [c]Wyss Institute for Biologically Inspired Engineering, Harvard University, Boston, MA 02115; [d]Focused Ultrasound Laboratory, Department of Radiology, Brigham and Women's Hospital, Harvard Medical School, Boston, MA 02115; [e]Laboratory of Nanotechnology for Precision Medicine, Istituto Italiano di Tecnologia, 16163 Genova, Italy; [f]DWI–Leibniz Institute for Interactive Materials, Rheinisch-Westfälische Technische Hochschule Aachen University, 52074 Aachen, Germany; [g]Institute of Technical and Macromolecular Chemistry, Polymeric Biomaterials, Rheinisch-Westfälische Technische Hochschule University Aachen, 52074 Aachen, Germany; [h]Department of Obstetrics and Gynecology, Medical Faculty, Rheinisch-Westfälische Technische Hochschule Aachen University, 52074 Aachen, Germany; and [i]Advanced Materials for Biomedicine, Institute of Applied Medical Engineering, Medical Faculty, Rheinisch-Westfälische Technische Hochschule Aachen University, 52074 Aachen, Germany

1. E. Stride *et al.*, Microbubble agents: New directions. *Ultrasound Med. Biol.* **46**, 1326–1343 (2020).
2. T. Opacic *et al.*, Motion model ultrasound localization microscopy for preclinical and clinical multiparametric tumor characterization. *Nat. Commun.* **9**, 1–13 (2018).
3. S. R. Sirsi, M. A. Borden, Microbubble compositions, properties and biomedical applications. *Bubble Sci. Eng. Technol.* **1**, 3–17 (2009).
4. T. Sun *et al.*, Closed-loop control of targeted ultrasound drug delivery across the blood–brain/tumor barriers in a rat glioma model. *Proc. Natl. Acad. Sci. U.S.A.* **114**, E10281–E10290 (2017).
5. N. Lipsman *et al.*, Blood–brain barrier opening in Alzheimer's disease using MR-guided focused ultrasound. *Nat. Commun.* **9**, 1–8 (2018).
6. J. N. May *et al.*, Multimodal and multiscale optical imaging of nanomedicine delivery across the blood-brain barrier upon sonopermeation. *Theranostics* **10**, 1948 (2020).
7. S. K. Wu *et al.*, Characterization of different microbubbles in assisting focused ultrasound-induced blood-brain barrier opening. *Sci. Rep.* **7**, 1–11 (2017).
8. S. Y. Wu, C. C. Chen, Y. S. Tung, O. O. Olumolade, E. E. Konofagou, Effects of the microbubble shell physicochemical properties on ultrasound-mediated drug delivery to the brain. *J. Control. Release* **212**, 30–40 (2015).
9. K. Kooiman, M. Foppen-Harteveld, A. F. van der Steen, N. de Jong, Sonoporation of endothelial cells by vibrating targeted microbubbles. *J. Control. Release* **154**, 35–41 (2011).
10. K. H. Song *et al.*, Microbubble gas volume: A unifying dose parameter in blood-brain barrier opening by focused ultrasound. *Theranostics* **7**, 144 (2017).
11. R. A. Barmin *et al.*, Engineering the acoustic response and drug loading capacity of PBCA-based polymeric microbubbles with surfactants. *Mol. Pharm.* **19**, 3256–3266 (2022).
12. S. Snipstad *et al.*, Sonopermeation to improve drug delivery to tumors: From fundamental understanding to clinical translation. *Expert Opin. Drug Deliv.* **15**, 1249–1261 (2018).
13. S. Snipstad *et al.*, Ultrasound and microbubbles to beat barriers in tumors: Improving delivery of nanomedicine. *Adv. Drug Deliv. Rev.* **177**, 113847 (2021).

14. J. A. Champion, S. Mitragotri, Role of target geometry in phagocytosis. *Proc. Natl. Acad. Sci. U.S.A.* **103**, 4930–4934 (2006).
15. J. A. Champion, S. Mitragotri, Shape induced inhibition of phagocytosis of polymer particles. *Pharm. Res*. **26**, 244–249 (2009).
16. F. J. Almgren, J. E. Taylor, The geometry of soap films and soap bubbles. *Sci. Am.* **235**, 82–93 (1976).
17. J. A. Champion, Y. K. Katare, S. Mitragotri, Making polymeric micro-and nanoparticles of complex shapes. *Proc. Natl. Acad. Sci. U.S.A.* **104**, 11901–11904 (2007).
18. N. Kapate, J. R. Clegg, S. Mitragotri, Non-spherical micro-and nanoparticles for drug delivery: Progress over 15 years. *Adv. Drug Deliv. Rev.* **177**, 113807 (2021).
19. P. Koczera *et al.*, PBCA-based polymeric microbubbles for molecular imaging and drug delivery. *J. Control. Release* **259**, 128–135 (2017).
20. M. Liu *et al.*, Drug loading in poly (butyl cyanoacrylate)-based polymeric microbubbles. *Mol. Pharm.* **17**, 2840–2848 (2020).
21. D. R. Morel *et al.*, Human pharmacokinetics and safety evaluation of SonoVue™, a new contrast agent for ultrasound imaging. *Invest. Radiol.* **35**, 80 (2000).
22. R. K. Kulkarni, H. J. Porter, F. Leonard, Glass transition temperatures of poly (alkyl α-cyanoacrylates). *J. Appl. Polym. Sci.* **17**, 3509–3514 (1973).
23. E. Stride, M. Edirisinghe, Novel microbubble preparation technologies. *Soft Matter* **4**, 2350–2359 (2008).
24. E. Stride, M. Edirisinghe, Novel preparation techniques for controlling microbubble uniformity: A comparison. *Med. Biol. Eng. Comput.* **47**, 883–892 (2009).
25. M. Aryal, C. D. Arvanitis, P. M. Alexander, N. McDannold, Ultrasound-mediated blood–brain barrier disruption for targeted drug delivery in the central nervous system. *Adv. Drug Deliv. Rev.* **72**, 94–109 (2014).
26. A. Guckenberger, S. Gekle, A boundary integral method with volume-changing objects for ultrasound-triggered margination of microbubbles. *J. Fluid Mech.* **836**, 952–997 (2018).
27. P. Dayton, A. Klibanov, G. Brandenburger, K. Ferrara, Acoustic radiation force in vivo: A mechanism to assist targeting of microbubbles. *Ultrasound Med. Biol.* **25**, 1195–1201 (1999).
28. S. Zhao *et al.*, Radiation-force assisted targeting facilitates ultrasonic molecular imaging. *Mol. Imaging* **3**, 135–148 (2004).
29. S. Y. Lee, M. Ferrari, P. Decuzzi, Shaping nano-/micro-particles for enhanced vascular interaction in laminar flows. *Nanotechnology* **20**, 495101 (2009).
30. F. Gentile, A. Curcio, C. Indolfi, M. Ferrari, P. Decuzzi, The margination propensity of spherical particles for vascular targeting in the microcirculation. *J. Nanobiotechnol.* **6**, 1–9 (2008).
31. M. Cooley *et al.*, Influence of particle size and shape on their margination and wall-adhesion: Implications in drug delivery vehicle design across nano-to-micro scale. *Nanoscale* **10**, 15350–15364 (2018).
32. D. Katanov, G. Gompper, D. A. Fedosov, Microvascular blood flow resistance: Role of red blood cell migration and dispersion. *Microvasc. Res.* **99**, 57–66 (2015).
33. A. J. Thompson, E. M. Mastria, O. Eniola-Adefeso, The margination propensity of ellipsoidal micro/nanoparticles to the endothelium in human blood flow. *Biomaterials* **34**, 5863–5871 (2013).
34. C. Xu, D. M. Wootton, Platelet near-wall excess in porcine whole blood in artery-sized tubes under steady and pulsatile flow conditions. *Biorheology* **41**, 113–125 (2004).
35. R. H. Phibbs, Distribution of leukocytes in blood flowing through arteries. *Am. J. Physiol.* **210**, 919–925 (1966).
36. D. S. Kohane, Microparticles and nanoparticles for drug delivery. *Biotechnol. Bioeng.* **96**, 203–209 (2007).
37. K. Yanagisawa, F. Moriyasu, T. Miyahara, M. Yuki, H. Iijima, Phagocytosis of ultrasound contrast agent microbubbles by Kupffer cells. *Ultrasound Med. Biol.* **33**, 318–325 (2007).
38. S. Garg, A. A. Thomas, M. A. Borden, The effect of lipid monolayer in-plane rigidity on in vivo microbubble circulation persistence. *Biomaterials* **34**, 6862–6870 (2013).
39. D. McMahon, A. Lassus, E. Gaud, V. Jeannot, K. Hynynen, Microbubble formulation influences inflammatory response to focused ultrasound exposure in the brain. *Sci. Rep.* **10**, 1–15 (2020).
40. J. A. Navarro-Becerra, K. H. Song, P. Martinez, M. A. Borden, Microbubble size and dose effects on Pharmacokinetics. *ACS Biomater. Sci. Eng.* **8**, 1686–1695 (2022).
41. E. Ben-Akiva *et al.*, Biomimetic anisotropic polymeric nanoparticles coated with red blood cell membranes for enhanced circulation and toxin removal. *Sci. Adv.* **6**, eaay9035 (2020).
42. K. T. Warzecha *et al.*, Targeting and modulation of liver myeloid immune cells by hard-shell microbubbles. *Adv. Biosyst.* **2**, 1800002 (2018).
43. C. Ergen *et al.*, Targeting distinct myeloid cell populations in vivo using polymers, liposomes and microbubbles. *Biomaterials* **114**, 106–120 (2017).
44. Y. Zhao *et al.*, A comparison between sphere and rod nanoparticles regarding their in vivo biological behavior and pharmacokinetics. *Sci. Rep.* **7**, 1–11 (2017).
45. A. Dasgupta *et al.*, Ultrasound-mediated drug delivery to the brain: Principles, progress and prospects. *Drug Discov. Today Technol.* **20**, 41–48 (2016).
46. S. Y. Wu, C. C. Chen, Y. S. Tung, O. O. Olumolade, E. E. Konofagou, Effects of the microbubble shell physicochemical properties on ultrasound-mediated drug delivery to the brain. *J. Control. Release* **212**, 30–40 (2015).
47. D. Trinh *et al.*, Microbubble drug conjugate and focused ultrasound blood brain barrier delivery of AAV-2 SIRT-3. *Drug Deliv.* **29**, 1176–1183 (2022).
48. S. Wang, G. Samiotaki, O. Olumolade, J. A. Feshitan, E. E. Konofagou, Microbubble type and distribution dependence of focused ultrasound-induced blood–brain barrier opening. *Ultrasound Med. Biol.* **40**, 130–137 (2014).
49. A. Jafari Sojahrood *et al.*, Toward precisely controllable acoustic response of shell-stabilized nanobubbles: High yield and narrow dispersity. *ACS Nano* **15**, 4901–4915 (2021).
50. N. Doshi, A. S. Zahr, S. Bhaskar, J. Lahann, S. Mitragotri, Red blood cell-mimicking synthetic biomaterial particles. *Proc. Natl. Acad. Sci. U.S.A.* **106**, 21495–21499 (2009).
51. M. W. Kim *et al.*, Platelet-like gold nanostars for cancer therapy: The ability to treat cancer and evade immune reactions. *Front. Bioeng. Biotechnol.* **8**, 133 (2020).
52. M. G. Shapiro *et al.*, Biogenic gas nanostructures as ultrasonic molecular reporters. *Nat. Nanotechnol.* **9**, 311–316 (2014).
53. R. W. Bourdeau *et al.*, Acoustic reporter genes for noninvasive imaging of microorganisms in mammalian hosts. *Nature* **553**, 86–90 (2018).
54. A. Bar-Zion *et al.*, Acoustically triggered mechanotherapy using genetically encoded gas vesicles. *Nat. Nanotechnol.* **16**, 1403–1412 (2021).
55. C. Manneschi *et al.*, A microfluidic platform with permeable walls for the analysis of vascular and extravascular mass transport. *Microfluid. Nanofluidics* **20**, 1–12 (2016).
56. N. Di Lascio, C. Kusmic, F. Stea, F. Faita, Ultrasound-based pulse wave velocity evaluation in mice. *J. Vis. Exp.* **120**, e54362 (2017).